Steel and Composite Structures, *Vol. 32, No. 4 (2019) 467-478*
DOI: https://doi.org/10.12989/scs.2019.32.4.467

Mapping vertical bridge deformations to track geometry for high-speed railway

Hongye Gou [*1,2,3], Zhiwen Ran [1a], Longcheng Yang [1b], Yi Bao [1c] and Qianhui Pu [1d]

[1] *Department of Bridge Engineering, School of Civil Engineering, Southwest Jiaotong University, Chengdu 610031, China*
[2] *Key Laboratory of High-Speed Railway Engineering, Ministry of Education, Southwest Jiaotong University, Chengdu 610031, China*
[3] *Department of Civil, Environmental and Ocean Engineering, Stevens Institute of Technology, Hoboken, NJ 07030, USA*

(*Received September 19, 2018, Revised July 9, 2019, Accepted July 30, 2019*)

Abstract. Running safety and ride comfort of high speed railway largely depend on the track geometry that is dependent on the bridge deformation. This study presents a theoretical study on mapping the bridge vertical deformations to the change of track geometry. Analytical formulae are derived through the theoretical analysis to quantify the track geometry change, and validated against the finite element analysis and experimental data. Based on the theoretical formulae, parametric studies are conducted to evaluate the effects of key parameters on the track geometry of a high speed railway. The results show that the derived formulae provide reasonable prediction of the track geometry change under various bridge vertical deformations. The rail deflection increases with the magnitude of bridge pier settlement and vertical girder fault. Increasing the stiffness of the fasteners or mortar layer tends to cause a steep rail deformation curve, which is undesired for the running safety and ride comfort of high-speed railway.

Keywords: analytical model; bridge vertical deformation; high-speed railway; mapping relationship; track deformation; track geometry

1. Introduction

High-speed railway (HSR) improves the quality of life and facilitates economic growth in many countries, thus playing an increasingly important role in resolving traffic problems (Hu *et al*. 2014). With the rapid development of HSR, the running safety and ride comfort of HSR are attracting more attentions (Vega *et al*. 2012, Ju 2013, Doménech *et al*. 2014, Rocha *et al*. 2014). Among many factors that influence the running safety and ride comfort, the track geometry is one of the most significant factors (Hu *et al*. 2014). Due to the advantages such as minimizing the interruption of existing lines and occupation of land, bridges cover more than 50% HSR mileage in China. The track geometry of HSR is highly dependent on the residual vertical and lateral deformation of bridges, thus highly affecting the running safety and ride comfort of HSR (Hu *et al*. 2014). The deformations that include the pier settlement, girder deflection, rotation, etc., are long-standing and cumulative over time (Ju *et al*. 2014, Shao *et al*. 2016).

The effect of pier settlement on the running safety of trains was studied through finite element analysis of train-track-bridge interaction (Ju 2013). The variability of parameters related to the bridge, the track and the train is taken into account along with the existence of track irregularities to compare the efficiency of different probabilistic methodologies for the safety assessment of short span railway bridges (Rocha *et al*. 2015). Gou *et al*. (2018a-d, 2019a-b) established a three-dimensional finite element model of the bridge–vehicle coupling system and compared with actual test data to analyze the influence of the train speed on the dynamic responses of the bridge and the safety and ride comfort of trains. The running safety and ride comfort of trains that travel over multispan bridges with pier settlement and girder deflection were investigated (Ju *et al*. 2014, Yang *et al*. 2014). The dynamic response of a maglev vehicle traveling over guideway girders that underwent pier settlement was investigated (Yau 2009a, b). In addition to the finite element analyses, other numerical studies have been conducted to link the bridge deformations with track geometry (Ruge and Birk 2007, Ruge *et al*. 2009, Zhang *et al*. 2015, Yang and Jang 2016). A discrete element model was established to analyze the effect of stress distribution and cumulative deformation of ballast track on the track geometry; a relationship between track cumulative settlement and geometry irregularity was presented and studied the shear behavior of fresh and coal fouled ballast in direct shear testing (Lu and McDowell 2010, Ferellec and McDowell 2010, Tutumluer *et al*. 2013, Indraratna *et al*. 2014). For the reliability analysis of high-speed railway bridges, a stochastic model is proposed to account for the environmental impact of seasonal temperature changes on the bridge structure (Salcher *et al*. 2016). The above numerical methods have been demonstrated effective in analyzing the running safety and riding comfort of HSR under a certain bridge deformation. However, finite element model and discrete element model are exclusive for a

*Corresponding author, Ph.D., Professor,
E-mail: gouhongye@swjtu.edu.cn
[a] M.S., E-mail: 1770825442@qq.com
[b] M.s., E-mail: 1106461245@qq.com
[c] Assistant Professor, E-mail: yi.bao@stevens.edu
[d] Professor, E-mail: qhpu@vip.163.com

ISSN: 1229-9367 (Print), 1598-6233 (Online)

specific case of bridge deformations. Different numerical models must be established to analyze different bridges under different deformations.

An analytical model was proposed to link the pier settlement and rail deformation of HSR bridges (Chen *et al*. 2014). Guo *et al*. (2017) proposed a calculation method for the mapping relationship between rail deflection and subgrade settlement to investigate the effect of subgrade settlement on the track geometry of the slab track. An original scheme for the dynamic analysis of the vehicle–bridge interaction (VBI) between trains and curved in-plan bridges is proposed to analyze the interaction along the radial and torsional sense of curved bridges (Dimitrakopoulos and Zeng 2015). These theoretical tools are useful to evaluate the rail deformation of HSR subjected to the type of bridge deformation considered. However, only limited types of bridge deformations were investigated. There is a need to develop mathematical tools to understand running safety and ride comfort of HSR under different bridge deformations (Gou *et al*. 2018e).

This paper presents an analytical model to link various bridge vertical deformations and the track geometry of HSR. This presented analytical model is validated through finite element analysis and experimental testing. Based on the model, the influence of bridge vertical deformations on track geometry is quantitatively studied.

2. Analytical study

2.1 Description of the track structure

This research studies the China Railway Track System (CRTS) I slab ballastless track system, which includes base slabs, a cement-asphalt (CA) mortar layer, track slabs, and rails, as shown in Fig. 1. The convex retaining platform is arranged between the two track slabs to restrict the displacement of the track slab; the elastic layer is arranged around the convex retaining platform. The CA mortar layer that supports the track slab is placed on top of the base slab that is bonded on the bridge girder. The rail is installed on the track slab using fasteners. In the bridge with M spans, uneven pier settlement causes deformations in the base slab and in other components on top of the base slab due to the direct contact.

The following four assumptions are adopted in the analytical study:

(1) In a typical HSR bridge, the rigidity of the bridge is much larger than the rigidity of the track system (Wang et al. 2014). Thus, the deformation of the track system has negligible effect on the deformation of the bridge.
(2) Debonding between the base slab and bridge girder is neglected because the base slab is connected to the beam through embedded steel bars. Thus, the deformation of the base slab is consistent with the deformation of the bridge girder. For convenient description, hereafter, the base slab is considered a part of the bridge girder, and ‘bridge girder’ is used to represent both the bridge girder and base slab.
(3) The CA mortar layer and fasteners are modelled using linear springs that are continuously deployed along the rail (Chen *et al*. 2014).
(4) Gravity of the track system is negligible.

2.2 Modelling the track slab

The bridge has N track slabs supported by the CA mortar layer and subjected to concentrated forces from the fasteners. When the bridge has vertical deformation, the *m*-th track slab is subjected to n concentrated forces (P_{m1} to P_{mn}) from the fasteners and distributed reaction forces from the CA mortar layer (Fig. 2). The fastener forces divide the track slab into (*m*+1) lengths. Two local coordinate systems are introduced in Fig. 2, one for the *m*-th track slab and the other one for the bridge girder corresponding to the *m*-th track slab. The origin point of the coordinate system for the track slab is at the center of the cross section at the left end of the track slab; at the same cross section, the origin of the coordinate system for the bridge girder is defined at the center of bridge girder.

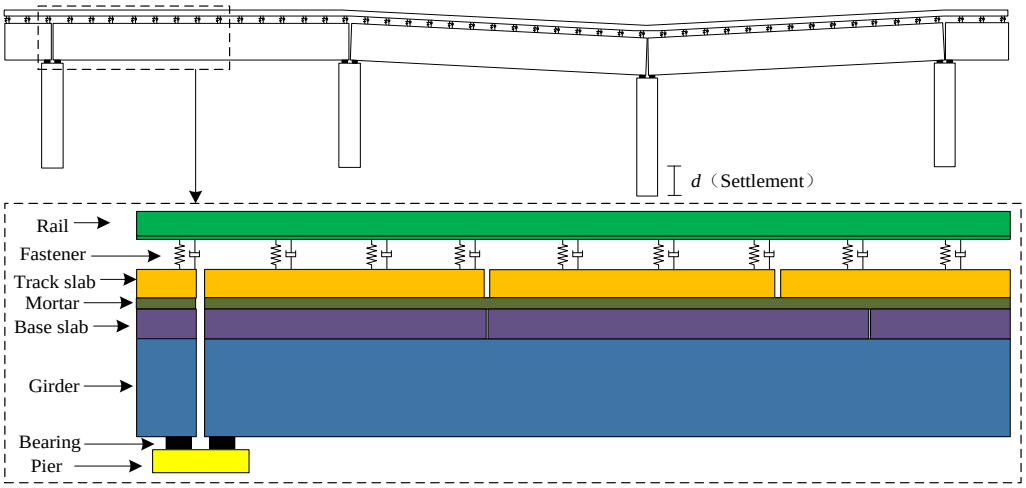

Fig. 1 Deformation of the CRTS I slab ballastless track under bridge pier settlement

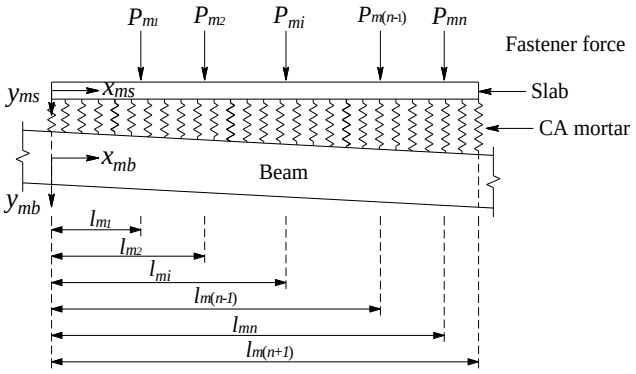

Fig. 2 Structural analysis diagram for the m-th track slab

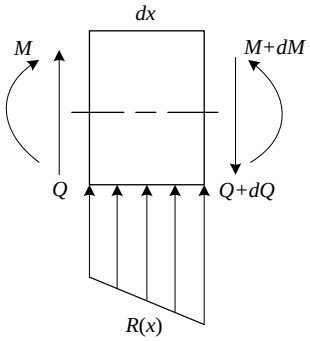

Fig. 3 Free-body diagram for the infinitesimal element of the slab under the fastener force

According to the principle of superposition, the deformation of track slab is determined by adding the deformations of the track slab caused by the fastener forces and interlayer action of mortar layer due to the relative displacement between track slab and base slab.

Fig. 3 shows the free-body diagram of an infinitesimal element (dx) of the m-th track slab under the action of fastener force. The internal loading includes the moment (M) and shear force (Q); the external loading includes a distributed load with a magnitude of $R(x)$ applied by the CA mortar layer.

The deformation of the track slab includes two parts, one part associated with the distributed spring forces $R(x)$, and the other part associated with the concentrated fastener forces (P_m). The spring force from the CA mortar layer is expressed as

$$R(x) = k_{cy} y(x) \tag{1}$$

where k_{cy} is the stiffness of the spring; $y(x)$ is the deformation of the spring, that is, the vertical relative displacement between the track slab and the base slab.

According to the differential equation of the deflection curve of girder and the force equilibrium condition of the infinitesimal element (dx), the deflection of the track slab associated with the distributed spring forces is expressed as

$$EI_s \frac{d^4 y}{dx^4} + k_{cy} y = 0 \tag{2}$$

The general solution of Eq. (2) is (Sun and Ren 2009)

$$\begin{aligned} y = {} & A_1 ch\lambda x \cos \lambda x + B_1 ch\lambda x \sin \lambda x \\ & + C_1 ch\lambda x \cos \lambda x + D_1 ch\lambda x \sin \lambda x \end{aligned} \tag{3}$$

where A_1, B_1, C_1 and D_1 are constants that are determined by boundary conditions; $\lambda = \sqrt[4]{\frac{k_{cy}}{4EI_s}}$.

At x = 0, the deflection, rotation angle, moment and shearing force of the track slab are

$$y = A(x) y_0 + B(x) \frac{\varphi_0}{\lambda} - C(x) \frac{M_0}{\lambda^2 EI_s} - D(x) \frac{Q_0}{\lambda^3 EI_s} \tag{4}$$

$$\begin{aligned} \varphi(x) = y' = {} & -4\lambda D(x) y_0 + \lambda A(x) \frac{\varphi_0}{\lambda} \\ & - \lambda B(x) \frac{M_0}{\lambda^2 EI_s} - \lambda C(x) \frac{Q_0}{\lambda^3 EI_s} \end{aligned} \tag{5}$$

$$\begin{aligned} M(x) = {} & EI_s 4\lambda^2 C(x) y_0 + EI_s 4\lambda^2 D(x) \frac{\varphi_0}{\lambda} \\ & + EI_s \lambda^2 A(x) \frac{M_0}{\lambda^2 EI_s} + EI_s \lambda^2 B(x) \frac{Q_0}{\lambda^3 EI_s} \end{aligned} \tag{6}$$

$$\begin{aligned} Q(x) = {} & EI_s 4\lambda^3 B(x) y_0 + EI_s 4\lambda^3 C(x) \frac{\varphi_0}{\lambda} \\ & - EI_s 4\lambda^3 D(x) \frac{M_0}{\lambda^2 EI_s} + EI_s \lambda^3 A(x) \frac{Q_0}{\lambda^3 EI_s} \end{aligned} \tag{7}$$

where

$$A(x) = ch\lambda x \cos \lambda x \quad B(x) = \frac{ch\lambda x \sin \lambda x + sh\lambda x \cos \lambda x}{2}$$

$$C(x) = \frac{ch\lambda x \sin \lambda x}{2} \quad D(x) = \frac{ch\lambda x \sin \lambda x - sh\lambda x \cos \lambda x}{4}$$

At the two ends of the track slab, the moment and shear force are zero

$$M(x = 0) = 0 \; ; \; Q(x = 0) = 0 \; ;$$
$$M\left(x = l_{m(n+1)}\right) = 0 \; ; Q\left(x = l_{m(n+1)}\right) = 0$$

The deformation of the track slab associated with the fastener forces at the i-th fastener of the m-th track slab (Fig. 2) is calculated using Eq. (8).

$$y^*_{msi} = A(l_{mi}) y^*_{ms0} + \frac{B(l_{mi})}{\lambda} \varphi^*_{ms0} - \sum_{j=1}^{i} \frac{D(l_{mi} - l_{mj})}{\lambda^3 EI_s} P_j \tag{8}$$

Under vertical deformations of the girder, relative displacement between the base slab and the track slab causes forces in the mortar layer. According to the equivalent force method, the effect of vertical deformation of the girder is simplified to the equivalent concentrated force acting on the track slab. The relative displacement between track slab and base slab is $y_{mb}(x)$; the concentrated

load is equal to $k_{cy}y_{mb}(x)dx$ in any small interval dx. The deformation value y^{+}_{msi} of the m-th track slab at the i-th fastener under the vertical deformation is

$$y^{+}_{msi} = A(l_{mi})y^{+}_{ms0} + \frac{B(l_{mi})}{\lambda}\varphi^{+}_{ms0} - \int_0^{l_{mi}} \frac{D(l_{mi}-x)}{\lambda^3 EI_s} k_{cy} y_{mb}(x)dx \tag{9}$$

Therefore, the total deformation of the m-th track slab at the i-th fastener is

$$\begin{aligned} y_{msi} &= y^{*}_{msi} + y^{+}_{msi} \\ &= A(l_{mi})y_{ms0} + \frac{B(l_{mi})}{\lambda}\varphi_{ms0} - \sum_{j=1}^{i} \frac{D(l_{mi}-l_{mj})}{\lambda^3 EI_s} P_j \\ &\quad - \int_0^{l_{mi}} \frac{D(l_{mi}-x)}{\lambda^3 EI_s} k_{cy} y_{mb}(x)dx \end{aligned} \tag{10}$$

Consequently, the deformation of the m-th track slab at all the fasteners is expressed in matrix form

$$\mathbf{[V_{ms}]=[R_m]+[D_m][P_m]} \tag{11}$$

where, $\mathbf{[V_{ms}]}$, $\mathbf{[R_m]}$, and $\mathbf{[P_m]}$ are $n\times1$ matrices; $\mathbf{[D_m]}$ is an $n\times n$ lower triangular matrices; the matrix elements are shown in Eqs. (12) to (15).

$$\mathbf{V_{ms}}(i,1) = y_{msi} \tag{12}$$

$$\mathbf{R_m}(i,1) = A(l_{mi})\eta_{m1} + B(l_{mi})\eta_{m2} - \int_0^{mi} \frac{D(l_{mi}-x)}{\lambda^3 EI_s} k_{cy} y_{mb} dx \tag{13}$$

$$\begin{aligned} &\mathbf{D_m}(i,j) = \\ &\frac{A(l_{mi})}{h_m EI_s}[D(l_{ms(n+1)})A(l_{ms(n+1)}-l_{msj}) - C(l_{ms(n+1)})B(l_{ms(n+1)}-l_{msj})] \\ &+ \frac{B(l_{mi})}{h_m}[B(l_{ms(n+1)})B(l_{ms(n+1)}-l_{msj}) - C(l_{ms(n+1)})A(l_{ms(n+1)}-l_{msj})] \\ &- \frac{D(l_{mi}-l_{mj})}{\lambda^3 EI_s} \end{aligned} \tag{14}$$

$$\mathbf{P}(i,1) = P_{mi} \tag{15}$$

The deformation of all the $M\times N$ track slabs is written as

$$\mathbf{[V_s]=[R]+[D][P]} \tag{16}$$

where, $\mathbf{[V_m]}$, $\mathbf{[R]}$ and $\mathbf{[P]}$ are *sum*×1-order matrices, $\mathbf{[D]}$ is an *sum*×*sum*-order matrices. The above matrices are composed of the vertical deformation value matrices from the first slab to the ($M\times N$)-th slab, the influence matrix of the vertical deformation of the bridge structure, the vertical force matrix of the fastener and the influence matrix of the fastener force of the slab vertical deformation. The individual elements are

$$\mathbf{[V_s]}=\begin{bmatrix}[V_{1s}]\\ M\\ [V_{ms}]\\ M\\ [V_{(M\times N)s}]\end{bmatrix}\quad \mathbf{[R]}=\begin{bmatrix}[R_1]\\ M\\ [R_m]\\ M\\ [R_{(M\times N)}]\end{bmatrix}\quad \mathbf{[P]}=\begin{bmatrix}[P_1]\\ M\\ [P_m]\\ M\\ [P_{(M\times N)}]\end{bmatrix}$$

$$\mathbf{[D]}=\begin{bmatrix}[D_1] & 0 & 0 & 0 & 0\\ 0 & O & 0 & 0 & 0\\ 0 & 0 & [D_m] & 0 & 0\\ 0 & 0 & 0 & O & 0\\ 0 & 0 & 0 & 0 & [D_{(M\times N)}]\end{bmatrix}$$

2.3 Modelling the rail

The rail is considered a girder supported on the track slab using sum number of fasteners that divide the rail into (*sum*+1) rail elements. Fig. 4 illustrates the deformation of the rail under the deformation of the track slab. A local coordinate system is introduced for the rail; the origin point of the coordinate system is at the center of the rail at the left end section. In the figure, the l_t represents the local coordinates of the t-th fastener.

The rail between the t-th and (t+1)-th rail elements is selected for mechanical analysis, as shown in Fig. 5. The internal loading includes the moment (M) and shear force (Q).

The deflection of the rail is expressed in Eq. (17)

$$-EI_s \frac{d^3 y}{dx^3} = Q_t \tag{17}$$

where the shear force Q_t is a constant when $X_r \in (l_t, l_{t+1})$; y can be written as a cubic polynomial of x

$$y = ax^3 + bx^2 + cx + d \tag{18}$$

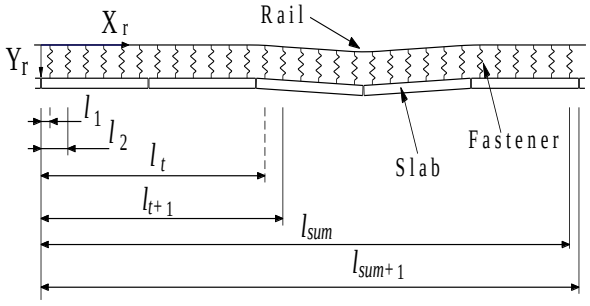

Fig. 4 Schematic diagram of the rail deformation

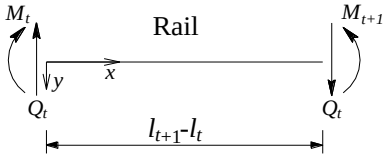

Fig. 5 Free-body diagram of a length of the rail

At $x = 0$, the deformation of the left end of the rail is y_t; the rotation angle is φ_t; the moment is M_t; the shear force is Q_t

$$y(x) = y_t + \varphi_t x - \frac{M_t}{2EI_r}x^2 - \frac{Q_t}{6EI_r}x^3 \tag{19}$$

$$\varphi(x) = \varphi_t - \frac{M_t}{EI_r}x - \frac{Q_t}{2EI_r}x^2 \tag{20}$$

$$M(x) = M_t + Q_t x \tag{21}$$

$$Q(x) = Q_t \tag{22}$$

The boundary conditions of the rail are

$$Y_{r0}(X_r = 0) = 0\ ;\ M_{r0}(X_r = 0) = 0\ ;$$
$$Y_{r0}(X_r = l_{sum+1}) = 0\ ;\ M_{r0}(X_r = l_{sum+1}) = 0$$

According to the principle of superposition, the rail deformation at the t-th fastener is

$$\begin{aligned} Y_{rt} = {} & l_t \sum_{k=1}^{sum} \frac{l_{sum+1}^2(l_{sum+1} - l_k) - (l_{sum+1} - l_k)^3}{6EI_r l_{sum+1}} P_k \\ & - l_t^3 \sum_{k=1}^{sum} \frac{(l_{sum+1} - l_k)}{6EI_r l_{sum+1}} P_k + \sum_{j=1}^{t} \frac{(l_t - l_k)^3}{6EI_r} P_k \end{aligned} \tag{23}$$

The deformation of the rail at all the fastener positions is expressed as

$$\mathbf{[V_r] = [L][P]} \tag{24}$$

where, $\mathbf{[V_r]}$ and $\mathbf{[L]}$ are $sum \times sum$-order matrices. The matrix elements are

$$\mathbf{V_r}(t,1) = Y_{rt} \tag{25}$$

$$\mathbf{L}(t,k) = \frac{[l_t l_{sum+1}^2(l_{sum+1} - l_k) - l_t(l_{sum+1} - l_k)^3 - l_t^3(l_{sum+1} - l_k) + (l_t - l_k)^3]}{(6l_{sum+1}EI_r)} \tag{26}$$

where $t \geq k$; $t = 1, 2, ..., sum$; $k = 1, 2, ..., sum$.

2.4 Linkage between bridge and track deformations

2.4.1 Mapping relationship

Relative displacement of rail and track slab produces fastener forces applied on the rail. The fastener force is expressed by Eq. (27)

$$\mathbf{[P]} = k_{fy}(\mathbf{[V_s]} - \mathbf{[V_r]}) \tag{27}$$

According to Eqs. (16) and (24), Eq. (27) can be rewritten as

$$\mathbf{[P]} = k_{fy}(\mathbf{[I]} + k_{fy}\mathbf{[L]} - k_{fy}\mathbf{[D]})^{-1}\mathbf{[R]} \tag{28}$$

According to Eqs. (24) and (28), the mapping relationship between the vertical deformation of the bridge and the track geometry at all the fastener positions is

$$\mathbf{[V_r]} = k_{fy}\mathbf{[L]}(\mathbf{[I]} + k_{fy}\mathbf{[L]} - k_{fy}\mathbf{[D]})^{-1}\mathbf{[R]} \tag{29}$$

The elements in the influence matrix **[R]** are only related to the function of the bridge structure deformation. Therefore, the influence of bridge pier settlement, girder vertical end rotation and fault on the track geometry is only reflected by **[R]**.

The rail vertical deformation can be solved by Eq. (30).

$$Y_{rt}(X_r) = \varphi_{r0}X_r - \frac{X_r^3}{6EI_r}Q_{r0} + \sum_{k=1}^{t}\frac{(X_r - l_k)^3}{6EI_r}P_k \tag{30}$$

where $l_t \leq X_r \leq l_{t+1}$, $t = 1, 2, ..., sum$.

From Eq. (29), the analytical matrix of the bridge structure vertical deformation maps to the rail surface can be determined by the influence matrix **[L]** of the fastener force of rail vertical deformation, the influence matrix **[D]** of the fastener force of slab vertical deformation, and the influence matrix **[R]** of the vertical deformation of the bridge structure. Given the HSR and the mechanical parameters of ballastless track, under different vertical deformation of the bridge, the influence matrix of the fastener force does not change.

2.4.2 Under pier settlement

When the pier on the right side of M_1-th span occurs a settlement of size d, the girder on both sides of the pier will follow the deformation. Fig. 6 shows the deformation diagram of girder due to the settlement of pier.

It can be seen from Fig. 6 that the vertical deformation of the girder of the M_1-th span is

$$Y_b = \frac{X_b - (M_1 - 1)L_b - L_{b0}}{L_b - 2L_{b0}}d \tag{31}$$

where $(M_1 - 1)L_b \leq X_b \leq M_1 L_b$.

Similarly, the vertical deformation of the girder of the $(M_1 + 1)$-th span is

$$Y_b = -\frac{X_b - (M_1 + 1)L_b - L_{b0}}{L_b - 2L_{b0}}d \tag{32}$$

where $M_1 L_b \leq X_b \leq (M_1 + 1)L_b$.

The vertical deformation of rest girder is zero. According to Eq. (13), the influence matrix **[R]** of the bridge vertical deformation is

$$\begin{aligned} \mathbf{R_m}(i,1) = {} & A(l_{mi})\eta_{m1} + B(l_{mi})\eta_{m2} \\ & - k_{cy}d\int_0^{l_{mi}} \frac{D(l_{mi} - x)[(X_b - L_m) - (M_1 - 1)L_b - L_{b0}]}{\lambda^3 EI_s(L_b - 2L_{b0})}dx \end{aligned} \tag{33}$$

where $\eta_{m1} = \frac{1}{h_m}\left[D(l_{ms(n+1)})f_{m2} - \lambda C(l_{ms(n+1)})f_{m1}\right]$;

$$\eta_{m2} = \frac{\lambda}{h_m}\left[\lambda B(l_{ms(n+1)})f_{m1} - C(l_{ms(n+1)})f_{m2}\right];$$

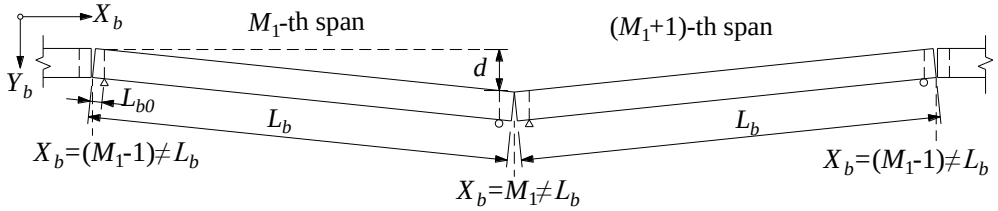

Fig. 6 Deformation of the girder under the pier settlement

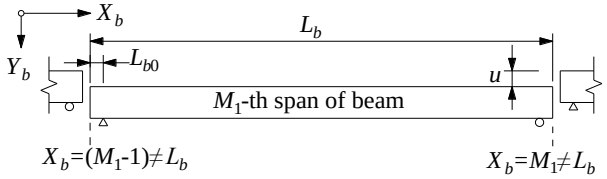

Fig. 7 Diagram of vertical girder fault

$$f_{m1}=\frac{k_{cy}d}{\lambda(L_b-2L_{b0})}\times \int_0^{l_{ms(n+1)}} B(l_{ms(n+1)}-x)[(X_b-L_m)-(M_1-1)L_b-L_{b0}]dx$$

$$f_{m2}=\frac{k_{cy}d}{L_b-2L_{b0}}\times \int_0^{l_{ms(n+1)}} A(l_{ms(n+1)}-x)[(X_b-L_m)-(M_1-1)L_b-L_{b0}]dx$$

According to Eq. (33), **[R]** can be divide into two parts

$$\mathbf{[R]}=\mathbf{[R_{se}]}d \tag{34}$$

where d is the bridge pier settlement; $\mathbf{[R_{se}]}$ is the remainder of the matrix **[R]**.

Plugging Eq. (34) into (28), the fastener vertical force matrix is rewritten as

$$\mathbf{[P]}=k_{fy}(\mathbf{[I]}+k_{fy}\mathbf{[L]}-k_{fy}\mathbf{[D]})^{-1}\mathbf{[R_{se}]}d \tag{35}$$

Plugging Eq. (34) into (29), the settlement of bridge piers is

$$\mathbf{[V_r]}=k_{fy}\mathbf{[L]}(\mathbf{[I]}+k_{fy}\mathbf{[L]}-k_{fy}\mathbf{[D]})^{-1}\mathbf{[R_{se}]}d \tag{36}$$

2.4.3 Under girder fault

When the girder of M_1-th span has vertical girder fault u, the rest of the bridge is not affected. The M_1-th span deformation is shown in Fig. 7.

The influence matrix **[R]** of the vertical deformation of the bridge structure is

$$\mathbf{R_m}(i,1)=A(l_{mi})\eta_{m1}+B(l_{mi})\eta_{m2}-k_{cy}u\int_0^{l_{mi}}\frac{D(l_{mi}-x)}{\lambda^3 EI_s}dx \tag{37}$$

where $\eta_{m1}=\frac{1}{h_m}\left[D(l_{ms(n+1)})f_{m2}-\lambda C(l_{ms(n+1)})f_{m1}\right]$;

$\eta_{m2}=\frac{\lambda}{h_m}\left[\lambda B(l_{ms(n+1)})f_{m1}-C(l_{ms(n+1)})f_{m2}\right]$;

$f_{m1}=k_{cy}u\int_0^{l_{ms(n+1)}}\frac{B(l_{ms(n+1)}-x)}{\lambda}dx$;

$f_{m2}=k_{cy}u\int_0^{l_{ms(n+1)}}A(l_{ms(n+1)}-x)dx$.

According to Eq. (37), **[R]** is decomposed into the product of the vertical girder fault u and $\mathbf{[R_{st}]}$, that is, **[R]** = $\mathbf{[R_{st}]}u$, where $\mathbf{[R_{st}]}$ is independent on u.

Therefore, when the bridge has a vertical girder fault u, the fastener vertical force matrix is

$$\mathbf{[P]}=k_{fy}(\mathbf{[I]}+k_{fy}\mathbf{[L]}-k_{fy}\mathbf{[D]})^{-1}\mathbf{[R_{st}]}u \tag{38}$$

The analytic matrix of the vertical girder fault mapping of the bridge to the rail deformation at all fastener positions is

$$\mathbf{[V_r]}=k_{fy}\mathbf{[L]}(\mathbf{[I]}+k_{fy}\mathbf{[L]}-k_{fy}\mathbf{[D]})^{-1}\mathbf{[R_{st}]}u \tag{39}$$

Based on the vertical force of the fastener obtained from Eq. (38), the analytical expression of the vertical deformation of the rail at any position is

$$Y_{rt}(X_r)=\varphi_{r0}X_r-\frac{X_r^3}{6EI_r}Q_{r0}+\sum_{k=1}^{t}\frac{(X_r-l_k)^3}{6EI_r}P_k \tag{40}$$

where $l_t \le X_r \le l_{t+1}$, t = 1, 2,..., *sum*.

3. Numerical study

3.1 Program implementation

According to the mapping relationship between the vertical deformation of the bridge and the track geometry, MATLAB is used to program the mapping relationship. The 5-span 32-m HSR bridge and the upper CRTS I slab ballastless track structure are analyzed to solve the rail deformation under the bridge pier settlement and the girder vertical fault deformation. The MATLAB program flow chart is shown in Fig. 8.

3.2 Finite element model

A three-dimensional (3D) finite element model is established using ANASYS for a five-span HSR bridge with CRTS I ballastless track slab, as shown in Fig. 9. Each span

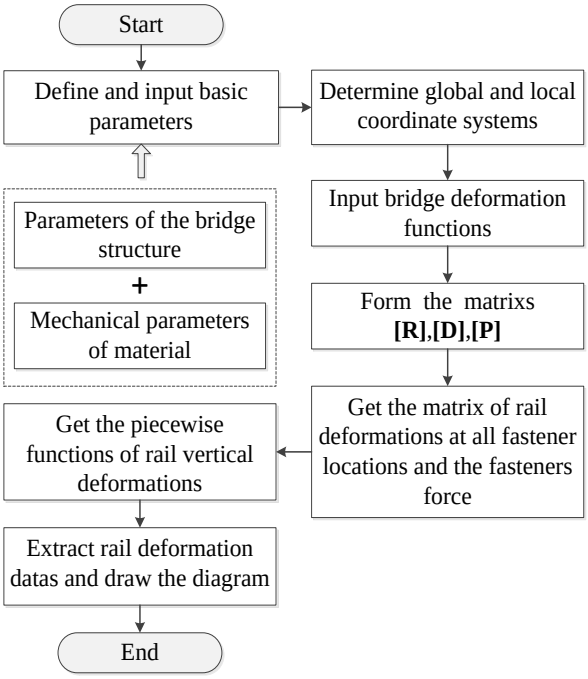

Fig. 8 Flow chart of the MATLAB codes for solving the equations

is 33 m long. The rail is simulated using 3D girder elements (GIRDER 188); the bridge girder, base slabs, track slabs, and the CA mortar layer are simulated using 3D solid elements (SOLID 45); the fasteners are simulated using 3D spring elements (COMBIN 14);. The bridge pier settlement and vertical girder fault are simulated through enforced deformations (Chen *et al*. 2014).

The materials and properties of different components of the bridge and track system are summarized in Table 1. The rail is made of U71MnG steel (Zhou *et al*. 2017). The bridge girder, base slab and track slab are made of reinforced concrete; different grades of concrete (C50, C40 and C60) are respectively used in different components (Chen *et al*. 2014), and the effect of reinforcement on the stiffness is neglected.

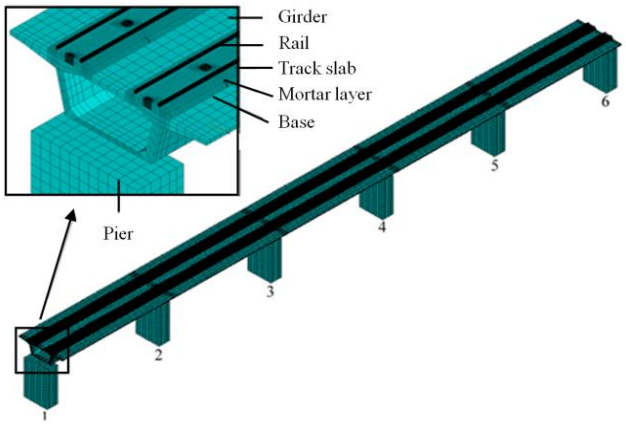

Fig. 9 Finite element model of a five-span HSR bridge with CRTS I ballastless track slab

3.3 Rail deformations under different bridge deformations

3.3.1 Pier settlement

A settlement of 5 mm is applied to the Pier 3 (Fig. 9). The finite element analysis and theoretical analysis results of the vertical deformation of the rail along the bridge is plotted in Fig. 10. The simulation and theoretical results agree well with each other at different locations of the bridge. The maximum discrepancy between the simulation and theoretical results is less than 5%. The rail deformation is consistent with the girder deformation.

The pier settlement causes additional forces in the fasteners, as shown in Fig. 11. The position fastener force represents tension force in the fasteners. The maximum discrepancy between the simulation and theoretical results is less than 2%. The fastener forces are symmetrical with respect to the settled pier. The pier settlement only affects the fastener forces in the two adjacent bridge spans, and the maximum fastener forces appear at the locations of the bridge piers in the two spans.

3.3.2 Vertical girder fault

A vertical girder fault of 3 mm is applied to the bridge span between the Pier 3 and Pier 4 (Fig. 9). The finite element analysis and theoretical analysis results of the

Table 1 Main calculation parameters of the CRTS I Ballastless track slab and the bridge

Components	Materials	Elastic modulus (GPa)	Poisson's ratio	Moment of inertia (mm^4)	Vertical spring stiffness (N/m)
Rail	U71MnG	210	0.3	3.217×10^7	—
Track slab	C60 concrete	36.5	0.2	1.372×10^9	—
Base slab	C40 concrete	34.0	0.2	1.867×10^9	—
Girder	C50 concrete	35.5	0.2	1.086×10^{13}	—
Convex retaining platform	C40 concrete	34.0	0.2	—	—
Elastic layer	Polyurethane resin	0.025	0.3	—	—
CA mortar layer	CA Mortar	0.2	0.2	—	9.0×10^8
Fastener	WJ-7B	—	—	—	3.0×10^7

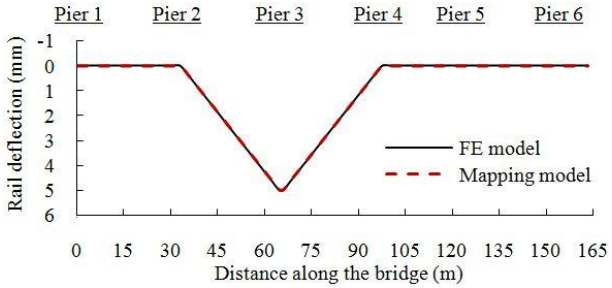

Fig. 10 Vertical rail deformation under a settlement of 5 mm

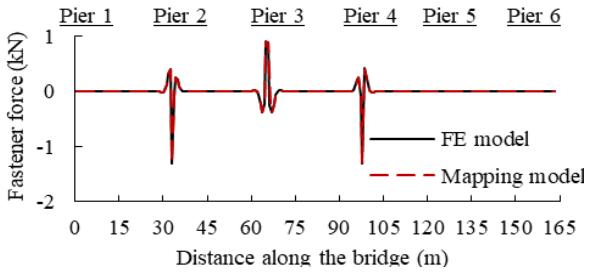

Fig. 11 Fastener force under a bridge pier settlement of 5 mm

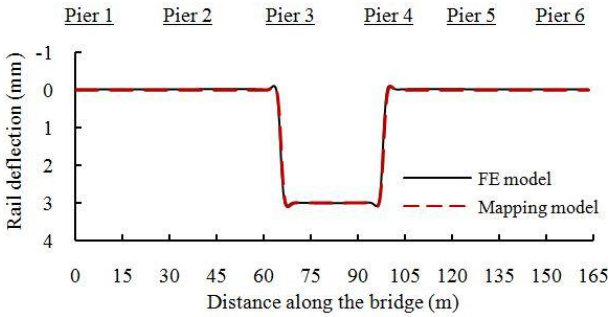

Fig. 12 Vertical rail deformation under a vertical girder fault of 3 mm

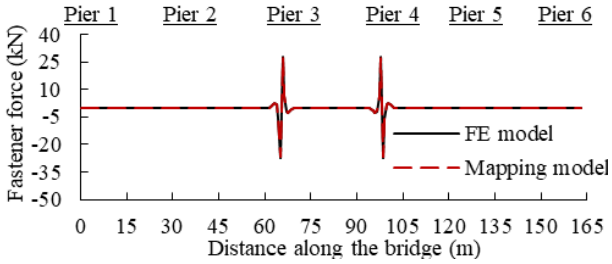

Fig. 13 Fastener force under 3 mm vertical girder fault

vertical deformation of the rail along the bridge is plotted in Fig. 12. The simulation and theoretical results agree well with each other at different locations of the bridge. The maximum discrepancy between the simulation and theoretical results is less than 5%. The rail deformation is consistent with the girder deformation.

The vertical girder fault causes additional forces in the fasteners, as shown in Fig. 13. The position fastener force represents tension force in the fasteners. The maximum discrepancy between the simulation and theoretical results is less than 2%. The fastener forces are symmetrical with respect to the mid-span of the bridge span (between Pier 3 and Pier 4) with the vertical fault. The vertical girder fault only affects the fasterner forces in the bridge span with the vertical fault, and the maximum fastener forces appear at the locations of the bridge piers in the span.

3.3.3 Elongation coefficient vertical girder fault

An elongation coefficient is introduced to evaluate the effects of different bridge deformations on the track geometry. The elongation coefficient is defined as the ratio

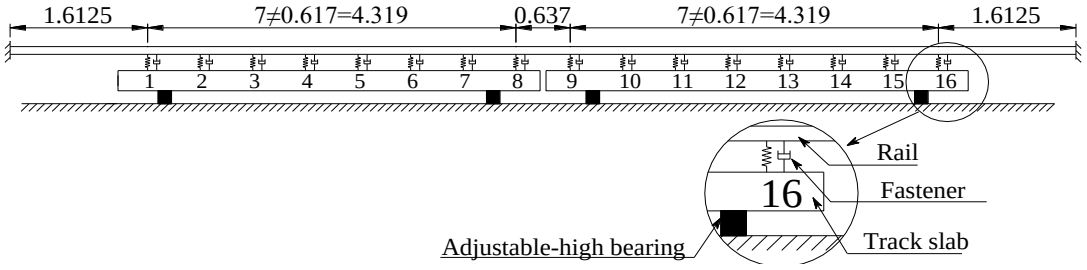

(a) Illustration of experimental device (unit: m)

(b) Photography of the rail and fastener arrangement

(c) Deployment of displacement sensors under the track slab

Fig. 14 Test track slab specimen and instrumentation

of the length of the rail deformation zone to the length of the girder deformation zone.

Take the bridge pier settlement of 3 mm and the vertical girder fault of 3 mm as examples, the elongation coefficient is 0.983 and 1.228, respectively, indicating that the mapping effect of the vertical girder fault is greater than that of the pier settlement on the track geometry.

4. Experimental study

The finite element model and theoretical analysis are compared with experimental results reported by Wei (2012). Fig. 14 shows the test track slab specimen and instrumentation. A pair of 12.5 m steel rail were installed on two track slabs using 16 fasteners, designated No. 1 to No 16. The track slabs were simply-supported on height adjustable bearings. A 0.5 mm vertical girder fault was created by adjusting the height of the bearing, as indicated in Fig. 14(a). Force transducers were used to measure the fastener forces in the fasteners No. 5 to No. 12. The deflection of the track slab was monitored using displacement sensors deployed under the track slab, as shown in Fig. 14(c).

Table 2 summarizes the material properties and section information of the rail, track slab, CA mortar layer and fasteners.

Fig. 15 shows the fastener forces for the fasteners No. 5 to No. 12. The finite element analysis and theoretical analysis results are compared with the experimental results reported by Wei (2012). The analysis results show reasonable agreement with the experimental results. The maximum fastener force predicted by the theoretical analysis is 4.45 kN, which is slightly higher than that (4.42 kN) predicted by the finite element model and also higher than the measured maximum force (3.12 kN) in the experiment. The discrepancy is primarily due to the change of the boundary conditions of the track slab. In the experiment, the CA mortar layer, base slab and bridge girder were replaced by the height adjustable bearings, which neglect the interlayer interaction provided by CA mortar layer and base slab thus resulting in the deviation between the experimental results and the mapping model results. The comparison result suggests that the theoretical analysis is more conservative than the simulation and experimental results.

Table 2 Calculation parameters of the mapping model

Structure	Elastic modulus (GPa)	Moment of inertia (mm^4)	Vertical spring stiffness (N/m)
Rail	210	3.217×10^7	—
Track slab	34.5	1.372×10^9	—
Mortar layer	—	—	4.5×10^8
Fastener	—	—	3.0×10^7

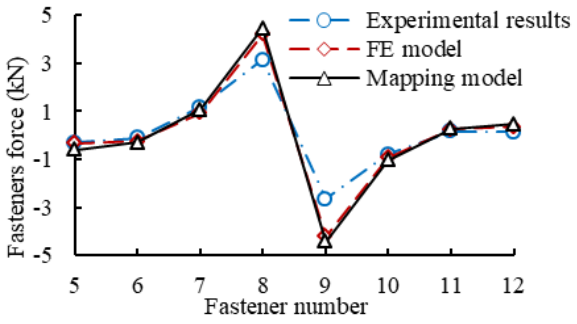

Fig. 15 Comparison of the experimental and theoretical results of the fastener forces under 0.5 mm vertical fault

5. Parametric studies

The validated theoretical formulae are then used to conduct parametric studies. The effects of pier settlement, vertical girder fault, stiffness of the fasteners, and stiffness of the CA mortar layer on the rail deflection are investigated.

5.1 Pier settlement

As the pier settlement is increased from 2 mm to 20 mm at the Pier 3 (Fig. 9), the rail deflection increases with the pier settlement within the Pier 2 and Pier 4, as shown in Fig. 16(a). The rail deflection is consistent with the pier settlement. The effects of pier settlement on the length of rail deformation zone and the elongation coefficient are shown in Fig. 16(b). As the pier settlement is increased from 2 mm to 20 mm, the length of rail deformation zone

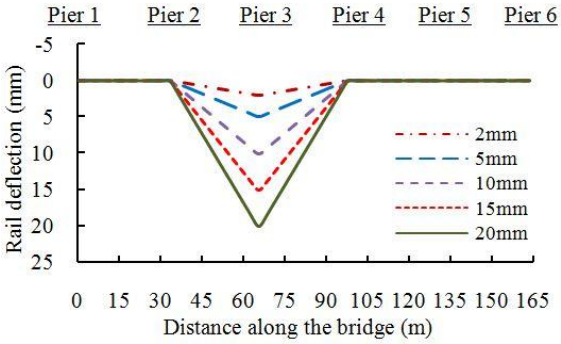

(a) Rail deflection along the bridge

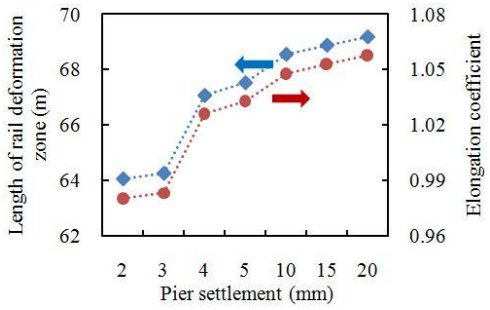

(b) The length of rail deformation zone and the elongation coefficient

Fig. 16 Effect of pier settlement on rail deflection

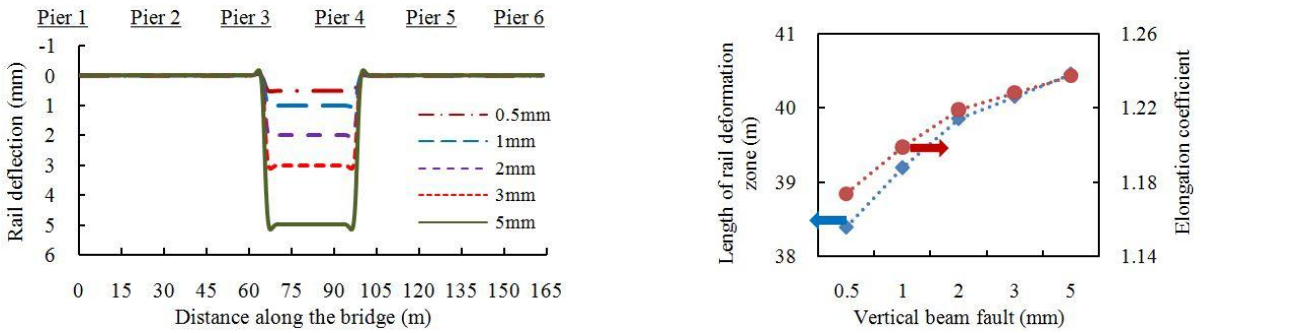

(a) Rail deflection along the bridge (b) The length of rail deformation zone and the elongation coefficient

Fig. 17 Effect of vertical girder fault on rail deflection

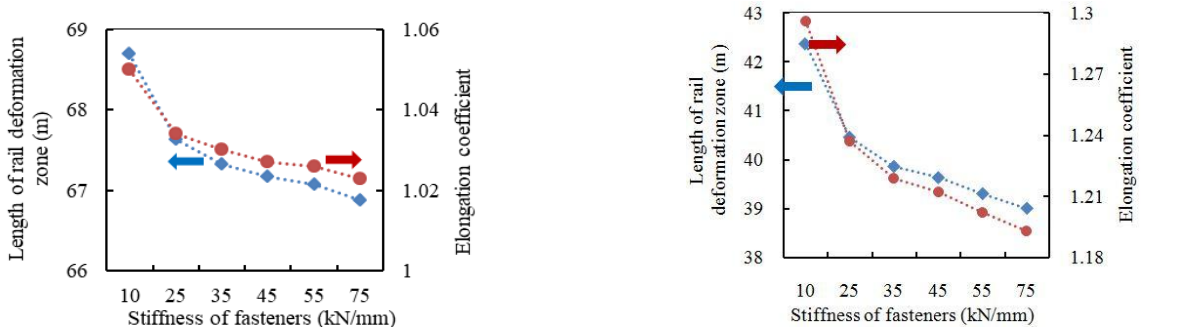

(a) Settlement of 5 mm at Pier 3 (b) Vertical girder fault of 3 mm between Pier 3 and Pier 4

Fig. 18 Effect of the stiffness of fasteners on the length of rail deformation zone and the elongation coefficient

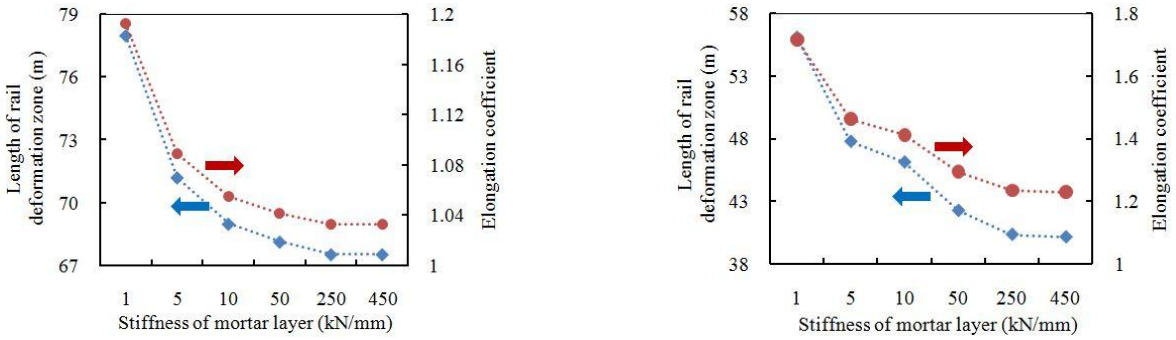

(a) Settlement of 5 mm at Pier 3 (b) Vertical girder fault of 3 mm between Pier 3 and Pier 4

Fig. 19 Effect of the stiffness of CA mortar on the length of the rail deformation zone and the elongation coefficient

increases from 64 mm to 69 mm (by 8%); the elongation coefficient increases from 0.98 to 1.06 (by 8%).

5.2 Vertical girder fault

As the vertical girder fault is increased from 0.5 mm to 5 mm in the span between the Pier 3 and Pier 4 (Fig. 9), the rail deflection increases with the vertical girder fault within the span, as shown in Fig. 17(a). The rail deflection is consistent with the vertical girder fault. The effects of vertical girder fault on the length of rail deformation zone and the elongation coefficient are shown in Fig. 17(b). As the vertical girder fault is increased from 0.5 mm to 5 mm, the length of rail deformation zone increases from 38.4 mm to 40.4 mm (by 5%); the elongation coefficient increases from 1.17 to 1.24 (by 6%).

5.3 Stiffness of the fasteners

As the tensile stiffness of the fasteners is increased from 10 kN/mm to 75 kN/mm, the length of rail deformation zone and the elongation coefficient decrease monotonically, as shown in Figs. 18(a) and (b). Under the settlement of 5 mm at Pier 3, as the stiffness of fasteners is increased from 10 kN/mm to 75 kN/mm, the length of rail deformation zone decreases from 68.7 mm to 66.9 mm (by 3%); the elongation coefficient decreases from 1.05 to 1.02 (by 3%). Under the vertical girder fault of 3 mm between Pier 3 and

Pier 4, as the stiffness of fasteners is increased from 10 kN/mm to 75 kN/mm, the length of rail deformation zone decreases from 42.4 mm to 39.0 mm (by 8%); the elongation coefficient decreases from 1.30 to 1.19 (by 9%).

5.4 Stiffness of the CA mortar layer

As the stiffness of the CA mortar layer is increased from 1 kN/mm to 450 kN/mm, the length of rail deformation zone and the elongation coefficient decrease monotonically, as shown in Figs. 19(a) and (b). Under the settlement of 5 mm at Pier 3, as the stiffness of fasteners is increased from 1 kN/mm to 450 kN/mm, the length of rail deformation zone decreases from 78.0 mm to 67.5 mm (by 13%); the elongation coefficient decreases from 1.19 to 1.03 (by 13%). Under the vertical girder fault of 3 mm between Pier 3 and Pier 4, as the stiffness of fasteners is increased from 1 kN/mm to 450 kN/mm, the length of rail deformation zone decreases from 56.1 mm to 40.2 mm (by 28%); the elongation coefficient decreases from 1.72 to 1.23 (by 28%).

6. Conclusions

Based on the above investigation, the following conclusions can be drawn:

- The rail deformation is consistent with the girder deformation in the bridge deformation area and decreased remarkably when the analyzed rail area is away from the bridge deformation zone.
- The mapping effects of different modes of bridge vertical deformation on the track geometry are different. Under the same conditions, the mapping effect of the vertical girder fault on the track geometry is greater than the pier settlement.
- The maximum value of the rail deformation increases with the amplitude of bridge deformation. The shape of rail deformation curve is dependent on the stiffness of fasteners and the mortar layer. Increasing the stiffness of fasteners and/or mortar layer tends to cause a steeper rail deformation curve, which is less desired for the running safety and ride comfort of HSR.

The analytical formulae of rail deformation established in this paper are mainly for CRTS I slab ballastless track. For other types of ballastless track structure, the analytical formula of rail deformation derived is different because of the difference in structure.

Acknowledgments

The research was funded by the National Natural Science Foundation of China (Grant No. 51878563), the Sichuan Science and Technology Program (Grant No. 2018JY0294 and 2018JY0549), and the Ministry of Science and Technology of China (Grant No. KY201801005).

References

Chen, Z.W., Sun, Y. and Zhai, W.M. (2014), "Mapping relationship between pier settlement and rail deformation of high-speed railways-part (I): The unit slab track system", *Sci. China*: *Tech. Sci*., **44**(7), 770-777. [In Chinese] https://doi.org/10.1360/N092014-00105

Dimitrakopoulos, E.G. and Zeng, Q. (2015), "A three-dimensional dynamic analysis scheme for the interaction between trains and curved railway bridges", *Comput. Struct*., **149**, 43-60. https://doi.org/10.1016/j.compstruc.2014.12.002

Doménech, A., Museros, P. and Martínez-Rodrigoa, M.D. (2014), "Influence of the vehicle model on the prediction of the maximum bending response of simply-supported bridges under high-speed railway traffic", *Eng. Struct*., **72**, 123-139. https://doi.org/10.1016/j.engstruct.2014.04.037

Ferellec, J.F. and McDowell, G.R. (2010), "A method to model realistic particle shape and inertia in DEM", *Granul. Matter*, **12**(5), 459-467. https://doi.org/10.1007/s10035-010-0205-8

Gou, H.Y., He, Y.N., Zhou, W., Bao, Y. and Chen, G.D. (2018a), "Experimental and numerical investigations of the dynamic responses of an asymmetrical arch railway bridge", *P. I. Mech. Eng. F-J. RAI*., **232**(9), 2309-2323.

Gou, H.Y., Long, H., Bao, Y., Chen, G.D., Pu, Q.H. and Kang, R. (2018b), "Experimental and numerical studies on stress distributions in girder-arch-pier connections of long-span continuous rigid frame arch railway bridge", *J. Bridge Eng*., **23**(7), 04018039. https://doi.org/10.1177/0954409718766929

Gou H.Y., Wang, W., Shi, X.Y., Pu, Q.H. and Kang, R. (2018c), "Behavior of steel-concrete composite cable anchorage system", *Steel Compos. Struct*., *Int. J*., **26**(1), 115-123. https://doi.org/10.12989/scs.2018.26.1.115

Gou, H.Y., Zhou, W., Chen, G.D., Bao, Y. and Pu, Q.H. (2018d), "In-situ test and dynamic analysis of a double-deck tied-arch bridge", *Steel Compos. Struct*., *Int. J*., **27**(1), 161-175. https://doi.org/10.12989/scs.2018.27.2.161

Gou, H.Y., Yang, L.C., Leng, D., Bao, Y. and Pu, Q.H. (2018e), "Effect of bridge lateral deformation on track geometry of high-speed railway", *Steel Compos. Struct*., *Int. J*., **29**(2), 219-229. https://doi.org/10.12989/scs.2018.29.2.219

Gou, H.Y., Long, H., Bao, Y., Chen, G.D. and Pu, Q.H. (2019a), "Dynamic behavior of hybrid framed arch railway bridge under moving trains", *Struct. Infrastruct. Eng*. https://doi.org/10.1080/15732479.2019.1594314

Gou, H.Y., Yang, L.C., Mo Z.X., Guo, W., Shi, X.Y. and Bao, Y. (2019b), "Effect of long-term bridge deformations on safe operation of high-speed railway and vibration of vehicle-bridge coupled system", *Int. J. Struct. Stab. Dyn.* https://doi.org/10.1142/S0219455419501116

Guo, Y., Gao, J.M., Sun, Y. and Zhai, W.M. (2017), "Mapping Relationship between Rail Deflection of Slab Track and Subgrade Settlement", *J. Southwest Jiaotong Univ*., **52**(6), 1139-1147. [In Chinese]

Hakim, S.J. and Razak, H.A. (2013), "Structural damage detection of steel bridge girder using artificial neural networks and finite element models", *Steel Compos. Struct, Int. J*.., **14**(4), 367-377. https://doi.org/10.12989/scs.2013.14.4.367

Hu, N., Dai, G.L., Yan, B. and Liu, K. (2014), "Recent development of design and construction of medium and long span high-speed railway bridges in China", *Eng. Struct*., **74**, 233-241. https://doi.org/10.1016/j.engstruct.2014.05.052

Hu, X.K., Xie, X., Tang, Z.Z., Shen, Y.G., Wu, P. and Song, L.F. (2015), "Case study on stability performance of asymmetric steel arch bridge with inclined arch ribs", *Steel Compos. Struct*., *Int. J*., **18**(1), 273-288. https://doi.org/10.12989/scs.2015.18.1.273

Indraratna, B., Ngo, N.T., Rujikiatkamjorn, C. and Vinod, J.S.

(2014), "Behaviour of fresh and fouled railway ballast subjected to direct shear testing: discrete element simulation", *Int. J. Geomech.*, **14** (1), 34-44. https://doi.org/10.1061/(ASCE)GM.1943-5622.0000264

Ju, S.H. (2013), "3D analysis of high-speed trains moving on bridges with foundation settlements", *Arch Appl. Mech.*, **83**(2), 281-291. https://doi.org/10.1007/s00419-012-0653-1

Ju, S.H, Leong, C.C. and Ho, Y.S. (2014), "Safety of maglev trains moving on bridges subject to foundation settlements and earthquakes", *J. Bridge Eng.*, **19**(1), 91-100. https://doi.org/10.1061/(ASCE)BE.1943-5592.0000506

Lu, M. and McDowell, G.R. (2010), "Discrete element modeling of railway ballast under monotonic and cyclic triaxial loading", *Géotechnique*, **60**(6), 459-467.

Rocha, J.M., Henriques, A.A. and Calcada, R. (2014), "Probabilistic safety assessment of a short span high-speed railway bridge", *Eng. Struct.*, **71**, 99-111. https://doi.org/10.1016/j.engstruct.2014.04.018

Rocha, J.M., Henriques, A.A., Calcada, R. and Rönnquist, A. (2015), "Efficient methodology for the probabilistic safety assessment of high-speed railway bridges", *Eng. Struct.*, **101**, 138-149. https://doi.org/10.1016/j.engstruct.2015.07.020

Ruge, P. and Birk, C. (2007), "Longitudinal forces in continuously welded rails on bridge decks due to nonlinear track-bridge interaction", *Comput. Struct.*, **85**(7), 458-475. https://doi.org/10.1016/j.compstruc.2006.09.008

Ruge, P., Widarda, D.R., Schmazlin, G. and Bagayoko, L. (2009), "Longitudinal track-bridge interaction due to sudden change of coupling interface", *Comput. Struct.*, **87**(1), 47-58. https://doi.org/10.1016/j.compstruc.2008.08.012

Salcher, P., Pradlwarter, H. and Adam, C. (2016), "Reliability assessment of railway bridges subjected to high-speed trains considering the effects of seasonal temperature changes", *Eng. Struct.*, **126**, 712-724. https://doi.org/10.1016/j.engstruct.2016.08.017

Shao, J.W., Zhao, D.X., Shu, L. and Shirley, J.D. (2016), "Safety and stability of light-rail train running on multispan bridges with deformation", *J. Bridge Eng.*, **21**(9), 06016004. https://doi.org/10.1061/(ASCE)BE.1943-5592.0000920

Sun, F.G. and Ren, L.N. (2009), "The operator solution of the fourth-order linear differential equation with varied coefficient", *J. Xi'an Polytechnic Univ.*, **23**(6), 142-146. [In Chinese]

Tutumluer, E., Qian, Y., Hashash, Y., Ghaboussi, J. and Davis, D.D. (2013), "Discrete element modelling of ballasted track deformation behavior", *Int. J. Rail Transport.*, **1**(1-2), 57-73. https://doi.org/10.1080/23248378.2013.788361

Vega, J., Fraile, A., Alarcon, E. and Hermanns, L. (2012), "Dynamic response of underpasses for high-speed train lines", *J. Sound Vib.*, **331**(23), 5125-5140. https://doi.org/10.1016/j.jsv.2012.07.005

Wang, P., Xu, J.H., Wang, L. and Chen, R. (2014), "Effect of track stiffness on frequency response of vehicle-track coupling system", *J. Railway Eng. Soc.*, **31**(9), 46-52. [In Chinese]

Wei, Y.H. (2012), "Research on girder end displacement relevant problems for high-speed railway ballastless track bridge", *China Academy of Railway Sciences*, Beijing, China. [In Chinese]

Xu, Y.L., Qian, Y., Song, G.B. and Guo, K.M. (2015), "Damage detection using finite element model updating with an improved optimization algorithm", *Steel Compos. Struct., Int. J.*, **19**(1), 191-208. https://doi.org/10.12989/scs.2015.19.1.191

Yang, S.C. and Jang, S.Y. (2016), "Track-bridge interaction analysis using interface elements adaptive to various loading cases", *J. Bridge. Eng.*, **21**(9), 04016056. https://doi.org/10.1061/(ASCE)BE.1943-5592.0000916

Yang, H., Chen, Z., Zhang, H. and Fan, J. (2014), "Dynamic analysis of train-rail-bridge interaction considering concrete creep of a multi-span simply supported bridge", *Adv. Struct. Eng.*, **17**(5), 709-720. https://doi.org/10.1260/1369-4332.17.5.709

Yau, J.D. (2009a), "Response of a maglev vehicle moving on a series of guideways with differential settlement", *J. Sound Vib.*, **324**(3), 816-831. https://doi.org/10.1016/j.jsv.2009.02.031

Yau, J.D. (2009b), "Response of a train moving on multi-span railway bridges undergoing ground settlement", *Eng. Struct.*, **31**(9), 2115-2122. https://doi.org/10.1016/j.engstruct.2009.03.019

Zhang, J., Wu, D.J. and Li, Q. (2015), "Loading-history-based track-bridge interaction analysis with experimental fastener resistance", *Eng. Struct.*, **83**, 62-73. https://doi.org/10.1016/j.engstruct.2014.11.002

Zhou, S.B., Zhang, Y.H., Zhang, G.Z., Shi, L.B. and Wang, W.J. (2017), "Friction and wear test of high speed wheel materials and U71MnG rail material", *Railway Eng.*, **57**(9), 128-131. [In Chinese]

CC